Modulating superexchange interactions in the two-dimensional high Curie temperature ferromagnetic semiconductors MoXY ($X =$ S, Se; $Y =$ Br, I)

Naibin Wang,[1] Junfeng Ren,[1,2,*] and Sai Lyu [1,2,†]

[1]*School of Physics and Electronics, Shandong Normal University, Jinan 250358, China*

[2]*Shandong Provincial Engineering and Technical Center of Light Manipulations & Institute of Materials and Clean Energy,*
Shandong Normal University, Jinan 250358, China

Two-dimensional ferromagnetic semiconductors are gaining increasing interest because of their promising applications in spintronics. However, the applications are greatly hindered by the weak ferromagnetic couplings and low Curie temperatures. Therefore, rationally designing two-dimensional ferromagnetic semiconductors with high Curie temperatures and enhancing their Curie temperatures are highly desirable, which inevitably requires a fundamental understanding of modulating superexchange interactions. Here, we propose two-dimensional intrinsic ferromagnetic semiconductors MoXY ($X =$ S, Se; $Y =$ Br, I). They are predicted to have unique quasi-1D transport behavior, high Curie temperatures (ranging from 290 K to 322 K), and large magnetic anisotropy energy. Based on the Kanamori's mechanism, we propose a general path-resolved indicator of the superexchange interaction strength to unravel how ferromagnetic superexchange interactions are modulated by two heavily used strategies, namely, ligand substitution and strain engineering. Our paper could provide a fundamental understanding of modulating superexchange interactions in two-dimensional ferromagnetic semiconductors.

I. INTRODUCTION

Inspired by the discovery of two-dimensional (2D) graphene [1], the family of 2D layered materials has been greatly expanded. For example, 2D transition-metal dichalcogenides can host all types of electronic states, such as insulators, semiconductors, metals, semimetals, etc. [1,2]. In this family, atomically thin materials with intrinsic magnetism have notably been missing until very recently [3–8]. According to the Mermin-Wagner-Hohenberg theorem [9,10], long-range magnetic ordering in 2D materials cannot exist at any finite temperature for isotropic Heisenberg models. It is magnetic anisotropy that breaks the condition of the Mermin-Wagner-Hohenberg therom and thus allows the existence of 2D magnetism [3,8]. Theoretical studies have been devoted to predicting stable 2D magnetic materials [11–14]. In 2017, the successful experimental demonstrations of 2D magnetism in CrI$_3$ and Cr$_2$Ge$_2$Te$_6$ stimulated intense research in this field [15,16].

Among the 2D magnets, 2D ferromagnetic (FM) semiconductors have attracted colossal attention because of their fundamental and technological importance [3,4]. On the one hand, 2D FM semiconductors provide platforms to investigate new physics, such as the magnetic proximity effect and the quantum anomalous Hall effect [17,18]. On the other hand, they are promising candidates for developing spintronics, which is crucial for next-generation information technology [8]. However, the Curie temperatures of currently available 2D FM semiconductors are usually considerably smaller than room temperature, which hinders the progress of spintronics development [3,19]. In addition, larger magnetic anisotropy energies (MAEs) usually indicate that magnetic ordering can have better resistance against thermal fluctuations. Therefore, there is a clear need to experimentally discover and/or theoretically predict 2D FM semiconductors with high Curie temperatures and large MAEs which can achieve robust FM couplings [5,8,20–23]. More importantly, there is growing interest in enhancing Curie temperatures of 2D FM semiconductors through various strategies, such as strain engineering, ligand modulation, etc. Unraveling the physics of how these strategies modulate the underlying superexchange interactions is key to rationally designing high-Curie temperature low-dimensional ferromagnets and enhancing their Curie temperatures, which has rarely been investigated [4,5,8]. For this aim, some indicators of superexchange interaction strengths have been proposed [5,21], but they are not path-resolved yet. For different superexchange paths, it is quite common that the superexchange interactions strengths have large variability in magnitude and behave differently under applied modulation strategies. Therefore, a path-resolved indicator of superexchange interaction strength is critical for the fundamental understanding of superexchange interaction under modulation strategies.

In this paper, we computationally predict orthorhombic 2D van der Waals (vdW) FM semiconductors MoXY ($X =$ S, Se; $Y =$ Br, I), which have high Curie temperatures and large MAEs and exhibit unique quasi-one-dimensional transport properties. Their stabilities are confirmed by phonon calculations and *ab initio* molecular dynamics (AIMD). The calculated Curie temperatures through Monte Carlo (MC) simulations range from 290 K (for MoSBr) to 322 K (for MoSeI). Furthermore, the Curie temperatures can be enhanced

*renjf@sdnu.edu.cn
†sailyu@sdnu.edu.cn

by ligand modulation and in-plane strain. According to the Kanamori's mechanism [24], we propose a path-resolved indicator of superexchange interaction strength by accounting for the major aspects. Then, we study the effects of two modulation strategies on both the superexchange and direct exchange interactions. By substituting ligand atoms from S to Se or Br to I, the FM superexchange interactions are found to be strengthened. In addition, the uniaxial tensile strain along the a or b axes weakens both the superexchange interactions and direct exchange interactions. This paper not only proposes an indicator of superexchange strength which can be directly applied to the study of other 2D FM semiconductors, but also provides a fundamental understanding on the physics behind modulating superexchange interactions through various strategies.

II. COMPUTATIONAL METHODS

The calculations of the electronic structure and the corresponding projected density of states (PDOS) are performed within the framework of density functional theory [25,26] as implemented in the QUANTUM ESPRESSO package [27]. The overlap matrices of the atomic orbitals are obtained as by-products of PDOS calculations. We adopt the Fritz-Haber-Institute type pseudopotentials [28] to describe the core-valence interaction and generalized gradient approximation (GGA) in the form of Perdew-Burke-Ernzerhof [29]. To account for the correlation effects of Mo-d electrons, the GGA + U method [30] is employed and the Hubbard U is chosen as 3 eV [31–34]. The dispersion correction method [35] is used to account for the long-range vdW interaction for the Mo XY monolayer. The thickness of the vacuum region is ~15 Å. The plane-wave energy cutoff is 60 Ry and the Monkhorst-Pack $\mathbf{k}$-point grid is set as $24 \times 16 \times 1$. To confirm the stabilities 2D Mo XY, we perform phonon calculations within the density functional perturbation theory (DFPT) method [36] and 5-ps AIMD at 300 K using the Nosé-Hoover method [37]. The on-site energies for the Mo-d orbitals are obtained using maximally localized Wannier functions, which are calculated by the WANNIER90 package [38]. To obtain the Curie temperatures, we first calculate exchange parameters from the total energy differences between several $2 \times 2 \times 1$ supercells with different magnetic phases. Then we use the VAMPIRE package [39] to calculate the temperature-dependent magnetization using the MC method [39–41]. The Curie temperatures are extracted by fitting the temperature-dependent magnetization to the Curie-Bloch function. When evaluating MAE, both the contributions from SOCs evaluated from relativistic pseudopotentials [42] and magnetic dipole-dipole interactions are taken into account.

III. RESULTS AND DISCUSSION

A. Electronic structure and quasi-1D electronic transport

The crystal structure of Mo XY corresponds to the orthorhombic space group $Pmmn$ [cf. Fig. 1(a)] and the choices of Cartesian axes are shown in Fig. 1(b). The structure is 2D and contains two molybdenum atoms, two chalcogenide atoms, and two halogen atoms in the unit cell. The unit cell
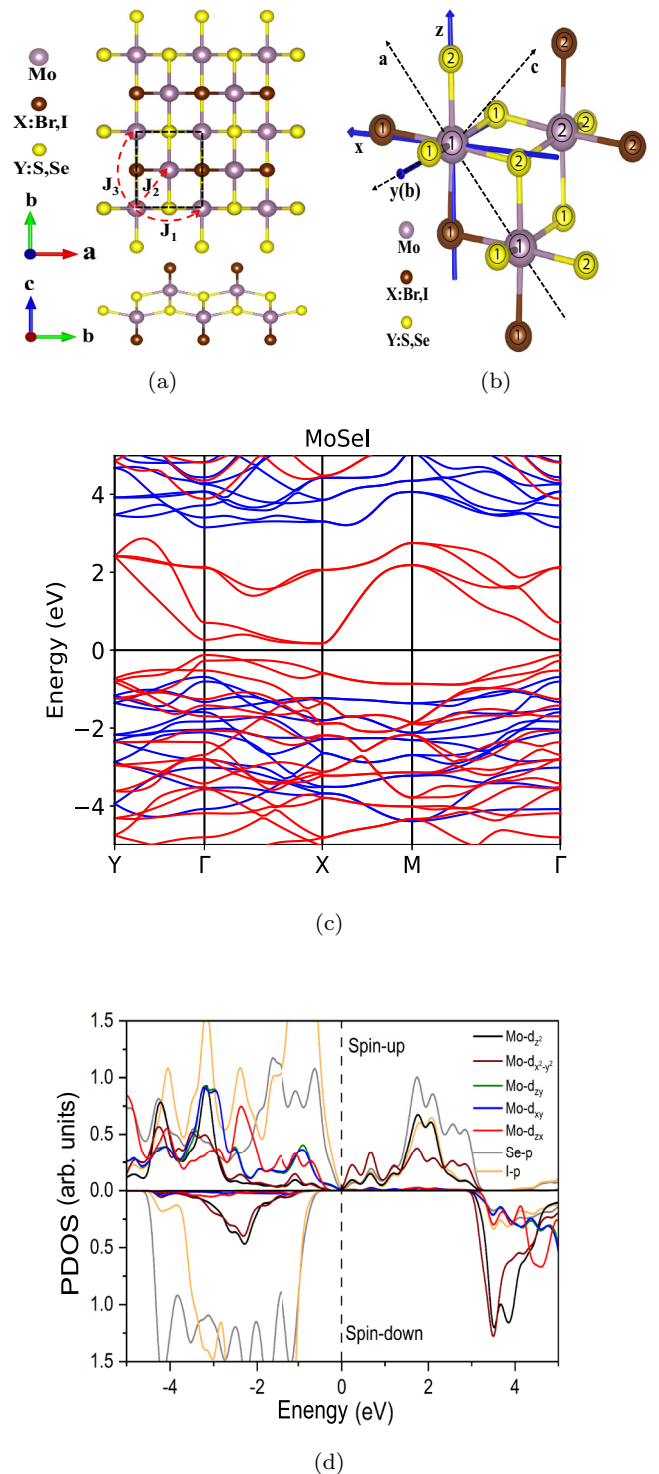

FIG. 1. (a) Top and side view of the MoXY monolayers; (b) the relations between the Cartesian axes and the crystallographic axes, (c) electronic band structure of MoSeI, and (d) PDOS of MoSeI.

contains two molybdenum-chalcogenide layers sandwiched in the two halogen layers. Surrounded by four chalcogenide atoms and two halogen atoms, each transition metal Mo atom occupies the center of a distorted octahedron. According to the electronegativities of these elements and the octet rule, each Mo atom tends to contribute three electrons to the nearby

TABLE I. Fully optimized lattice constants a and b, and the calculated direct and indirect band gaps (E_g and $E_{g,i}$) of 2D MoXY (X = S, Se; Y = Br, I) monolayers.

	a (Å)	b (Å)	E_g (eV)	$E_{g,i}$ (eV)
MoSBr	3.793	5.002	0.91	0.89
MoSI	3.923	4.995	0.80	0.71
MoSeBr	3.885	5.287	0.46	
MoSeI	4.020	5.279	0.39	0.30

TABLE II. Calculated effective masses m^* (in unit of electron mass), deformation potentials (E^P), elastic modulus (C_{2D}), and carrier mobilities (μ_{2D}) for MoXY (X=S, Se; Y=Br, I) monolayers at room temperature.

Carrier		Direction	m^*	E^p (eV)	C_{2D} (J/m^2)	μ_{2D} (cm^2 V^{-1} s^{-1})
MoSBr	h	Γ-X	1.53	9.56	177.90	47
		Γ-Y	0.22	8.63	140.94	314
	e	Γ-X	2.93	9.36	177.90	18
		Γ-Y	0.23	13.64	140.94	87
MoSI	h	Γ-X	2.01	7.28	91.78	24
		Γ-Y	0.28	7.59	118.59	209
	e	Γ-X	1.53	8.34	91.78	30
		Γ-Y	0.24	14.09	118.59	87
MoSeBr	h	Γ-X	1.48	9.64	101.24	34
		Γ-Y	0.15	7.70	115.55	594
	e	Γ-X	2.62	9.00	101.24	15
		Γ-Y	0.18	12.86	115.55	119
MoSeI	h	Γ-X	1.87	7.17	85.41	26
		Γ-Y	0.28	6.45	94.31	238
	e	Γ-X	1.19	7.43	85.41	57
		Γ-Y	0.20	12.74	94.31	127

chalcogenide and bromine atoms, resulting in Mo^{3+} cations, S^{2-} (or Se^{2-}) and Br$^-$ (or I$^-$) anions. The Hund's rule requires that the spins of the three remaining d-orbital electrons in each Mo^{3+} cation are the same. Based on the crystal field theory, the crystal field at the Mo^{3+} sites split the five $3d$ orbitals into two groups with different energies: e_g (d_{z^2} and $d_{x^2-y^2}$) and t_{2g} (d_{xy}, d_{yz}, and d_{zx}) orbitals. Thus, the three same-spin $3d$ electrons in each Mo^{3+} cation are expected to occupy the three energy-lower t_{2g} orbitals.

By performing total energy calculations for all possible FM and antiferromagnetic (AFM) states within a $2 \times 2 \times 1$ supercell, we confirm that the ground state of monolayer MoXY is FM. The optimized lattice parameters and the calculated band gaps are summarized in Table I. As expected, the lattice parameters slightly increase from MoSBr to MoSeI. The stabilities of the MoXY monolayers are confirmed by performing phonon calculations within DFPT and AIMD simulations, which are given in the Supplemental Material [43]. The spin-polarized electronic band structure and the corresponding PDOS of MoSeI and other monolayers obtained through GGA + U calculations are shown in Fig. 1 and Fig. S4 in the Supplemental Material [43], respectively. For MoSBr, MoSI, and MoSeI, the indirect gap is slightly smaller than the direct gap at the Γ point. The valence band maximum (VBM) is located at the Γ point, while the conduction band minimum (CBM) is located at between Γ and X. At variance, MoSeBr is found to be a direct-gap semiconductor. The gaps decrease as the in-plane area increases, indicating negative deformation potential.

MoXY monolayers exhibit unique quasi-1D transport behaviors. Their lowest conduction bands and highest valence bands in the vicinity of the Γ point are highly anisotropic along the two in-plane dimensions, i.e., the a and b directions. To be more specific, the nearly flat bands from Γ to X indicate quite low carrier mobilities. At variance, the steeper bands from Γ to Y imply higher carrier mobilities. To quantify this, we calculate the carrier mobilities based on the deformation potential theory using the following equation [44–47]:

$$\mu_{2D} = \frac{e\hbar^3 C_{2D}}{K_B T m^* \sqrt{m_a^* m_b^*}(E^P)^2},$$ (1)

where e is the elementary charge, $\hbar$ is the Planck's constant, C_{2D} is the elastic modulus, K_B is Boltzmann's constant, T is the temperature, m_a^* and m_b^* are the effective masses along the in-plane a and b directions, respectively, and m^* and E^P denote the effective mass and deformation potential along the transport direction, respectively. The calculated carrier mobilities for MoXY at room temperature are listed in Ta-

ble II. Clearly, the carrier mobilities along the b direction are significantly larger than those along the a direction. Thus, the carriers are highly localized along the a direction and the transport behavior along the b direction is quasi-one-dimensional. Such unique quasi-one-dimensional electronic transport behavior in MoXY monolayers can be understood in terms of tight-binding models and superexchange interactions. According to the PDOS [cf. Fig. 1(d)], the VBM for each material is mainly composed of the anion-p orbitals of the chalcogenide and halogen atoms. The superexchange interactions between the Mo cations and ligands in the ab plane require that the anion-p orbitals in the xz plane point toward the Mo cations [cf. Fig. 1(b)]. As a result, the directions of the anion-p orbitals form ~45° angles with the a direction. In the tight-binding picture, the overlapping integrals of the p orbitals along the a direction are considerably smaller than the overlapping integral of p_y orbitals along the b direction, leading to notably less dispersive bands and therefore larger effective masses and smaller hole mobilities. For the CBM at Γ, one can conduct a similar analysis. The CBM is mainly composed of the empty d orbitals of Mo, i.e., the e_g orbitals. Because of the ~45° angles with the a direction, the overlapping integrals of these orbitals along the a direction are comparatively smaller than those along the b direction as well. Interestingly, both CrSBr and CrSeBr exhibit the similar behavior [48,49]. We here provide the physical origin of this unique quasi-1D transport behavior, which could offer platforms to study how electrons behave in a one-dimensional environment and be useful alternatives for fabricating complicated one-dimensional devices, such as nanowires.

B. Competing magnetic mechanisms: Superexchange and direct exchange interactions

The origin of the FM ground states in MoXY (X = S, Se; Y = Br, I) monolayers are ascribed to the competitions

between superexchange and direct exchange interactions. At variance with short-ranged direct exchange interactions, superexchange interactions are mediated by the anion-p orbitals. For each Mo^{3+} ion, the t_{2g} orbitals are half filled with the same-spin electrons, while the e_g orbitals are empty. Therefore, the direct exchange interaction between two neighboring Mo^{3+} ions are AFM because the virtual electron transfers are suppressed between t_{2g} and e_g orbitals as required by the Pauli exclusion principle [50]. We first analyze the exchange interactions along the a direction pertinent to the exchange interaction parameter J_1. Based on the semiempirical Goodenough-Kanamori-Anderson (GKA) rules [24,51,52], the $\sim 90°$ Mo-anion-Mo superexchange interactions along the a direction result in FM couplings. According to the Kanamori's mechanism [24], the p_z (or p_x) orbitals of the corner-sharing anions couple to the Mo^{3+} d_{z^2} (or $d_{x^2-y^2}$) orbitals to form the partial covalent bonds, and the remaining anion-p_z (or p_x) orbitals with opposite spins overlap with the d_{zx} orbitals of the neighboring Mo^{3+} ion to give rise to the exchange integrals. In terms of Goodenough's mechanism, the corner-sharing anions couple to d_{z^2} of Mo on the one side via p_z and to $d_{x^2-y^2}$ of Mo on the other side via p_x. Because of the shorter lattice constant along the a direction, rather than those along the ab diagonal and b directions, the direct exchange interaction between each pair of two neighboring Mo^{3+} ions are expected to be most pronounced and counteract with the FM superexchange interactions. The $\sim 90°$ superexchange interactions along the ab diagonal directions correspond to the exchange interaction parameter J_2, for which there are two possible superexchange interaction paths. For the corner-sharing X atoms, their p_z (or p_x) orbitals hybridize with the Mo^{3+} d_{z^2} (or $d_{x^2-y^2}$) orbitals to form the partial covalent bonds, and the remaining p_z (or p_x) orbitals with opposite spins are nonorthogonal to the d_{yz} (or d_{xy}) orbitals of the neighboring Mo^{3+} ion and give rise to the exchange integrals. This results in FM couplings between the neighboring Mo^{3+} ions along the ab diagonal directions and therefore the positive sign of J_2. The Mo-X-Mo chain along the b direction is zigzag with a bond angle between $90°$ and $180°$ ($\sim 157°$), which brings about some overlaps between the X-p_y orbital and the Mo-t_{2g} orbitals. According to the GKA rules, the resulting superexchange interaction is weak FM. Both the superexchange and direct exchange interactions along the b direction are expected to be weaker than those along the ab diagonal direction and the a direction.

In Fig. 2, we schematically show the mechansims for the superexchange interactions and the direct exchange interactions between the Mo cations. Based on the Kanamori's mechanism, the strength of the superexchange interactions between two half-filled t_{2g} orbitals can be ascribed to two major aspects: electron transfer from anion-p_σ to cation-e_g orbitals to form partial covalent bonds and the exchange integrals between anion-p_σ and occupied cation-t_{2g} orbitals [24]. Consequently, more electrons transfer from anion-p_σ to cation-e_g orbitals and larger exchange integrals between anion-p_σ and occupied cation-t_{2g} orbitals indicate strong superexchange interactions. The integrated area for the occupied e_g orbitals in PDOS (hereinafter referred as Q_{ET}) can be used to account for the spin-up $p_\sigma - e_g$ covalency [21]. The exchange integrals between spin-down p_σ and t_{2g} orbitals can be assumed to be
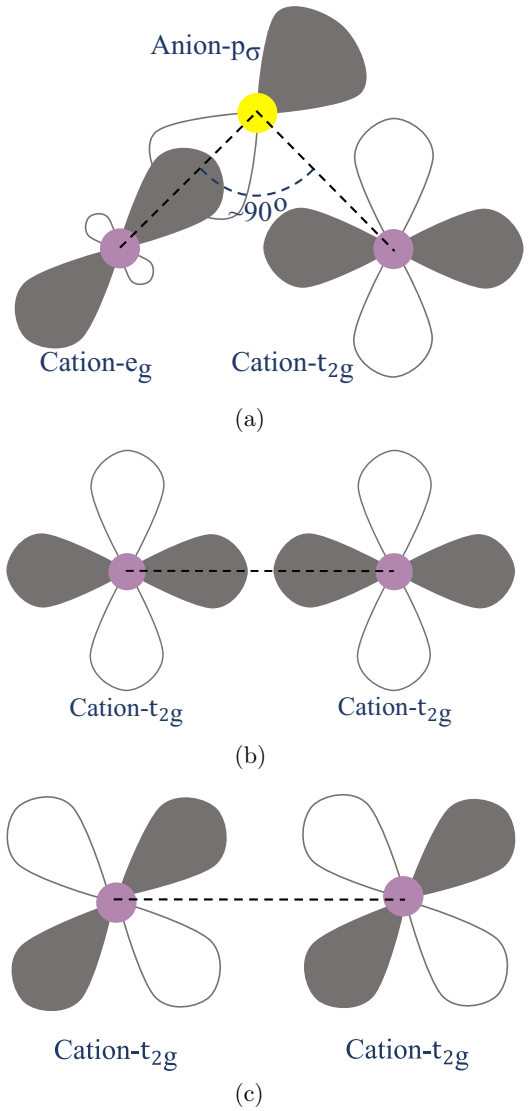

FIG. 2. Schematic representations for (a) the superexchange interactions according to Kanamori's superexchange mechanism and the direct exchange interactions (b) for J_1 and J_2 and (c) for J_3.

proportional to $-S^2/d$, where S is the orbital overlap and d is the distance between the anion and the cation [53]. This approximation tends to underestimate the exchange integral and hence overestimate the superexchange interaction strength for intermediate-angle (or even $180°$) cation-anion-cation interactions with small (or even zero) orbital overlaps [53]. Since our focus is on $90°$ cation-anion-cation interactions resulting in FM coupling with larger orbital overlaps, the approximation is expected to be valid. Therefore, we define the indicator for the strength of the superexchange interactions as

$$J^{\text{SE, ind}} \sim \Sigma Q_{\text{ET}}(e_g) \frac{S_{pd}^2(p_\sigma, t_{2g})}{d(p_\sigma, t_{2g})}, \tag{2}$$

where the sum runs over all the involved orbitals for a given superexchange path. The minus sign is dropped out due to the opposite spins of the two anion-p_σ orbitals involved in the interactions. This expression allows us to indicate the strengths of superexchange interactions for different paths.

TABLE III. Calculated exchange interaction parameters and Curie temperatures for MoXY ($X = $ S, Se; $Y = $ Br, I) monolayers.

	J_1 (meV)	J_2 (meV)	J_3 (meV)	J_{avg}(meV)	T_C (K)
MoSBr	4.3	7.5	8.5	6.95	290
MoSI	4.6	7.1	9.3	7.02	291
MoSeBr	6.4	9.0	5.5	7.48	301
MoSeI	7.0	8.8	7.1	7.93	322

C. Effects of ligand substitution and strain on Curie temperatures

To calculate the Curie temperatures in Mo XY monolayers, we first use the following Heisenberg-like Hamiltonian to describe the magnetic interactions between adjacent Mo^{3+} ions (S = 3/2):

$$H = -\sum_{\langle i,j \rangle} J_1 \vec{S}_i \cdot \vec{S}_j - \sum_{\langle k,l \rangle} J_2 \vec{S}_k \cdot \vec{S}_l - \sum_{\langle m,n \rangle} J_3 \vec{S}_m \cdot \vec{S}_n$$
$$+ D \sum_i \left(S_i^c\right)^2 + E \sum_i \left[\left(S_i^a\right)^2 - \left(S_i^b\right)^2\right], \quad (3)$$

where J_1, J_2, and J_3 are the isotropic Heisenberg exchange interaction constants for the first-, second-, and third-nearest-neighbors Mo^{3+}, respectively, and $\vec{S}$ is the spin vector of each magnetic ion. D and E are parameters to account for the magnetic anisotropy. Taking MoSeI as an example, the distances between the neighboring Mo atoms for the three J parameters are 4.02, 4.05, and 5.28 angstroms, respectively. Then, we calculate the exchange interaction constants from the energy differences between the FM ground state and the three AFM metastable states [Fig. S5(a) in the Supplemental Material [43]]. By performing $\sim 10^5$ iterations of MC simulations for a $75 \times 75 \times 1$ superlattice, we obtain the normalized magnetic moment as a function of temperature for each compound and then fit it to the Curie-Bloch function, i.e., $(1 - T/T_C)^\beta$, to extract the Curie temperature T_C (cf. Fig. S5(b) in the Supplemental Material [43]). The calculated exchange interaction parameters J and Curie temperatures for Mo XY monolayers are summarized in Table III. We also list the weighted averages of the exchange interaction parameters, which are defined as

$$J_{avg} = \frac{\Sigma_i n_i J_i}{\Sigma_i n_i}, \quad (4)$$

where n_i refers to the number of interaction pairs per unit cell for J_i. In this case, n_1, n_2, and n_3 are 1, 2, and 1, respectively. As expected, the Curie temperatures are proportional to the averaged exchange interaction constants.

The calculated Curie temperatures for MoXY monolayers range from 290 K to 322 K and are above room temperature. By varying ligands from S to Se or from Br to I, the electronegativities of the anions decrease and hence enhance the electron transfer from the anions to the cations. For the heavier ligands, the electrons from the anion-p_σ orbitals can more effectively hop to the cation-e_g orbitals and then lead to the benefited $p_\sigma - e_g$ covalency. The strength of covalency can be reflected by the integrated area of occupied spin-up e_g orbitals (cf. Fig. S7 in the Supplemental material). Meanwhile, the overlapping matrices between p_σ and t_{2g}
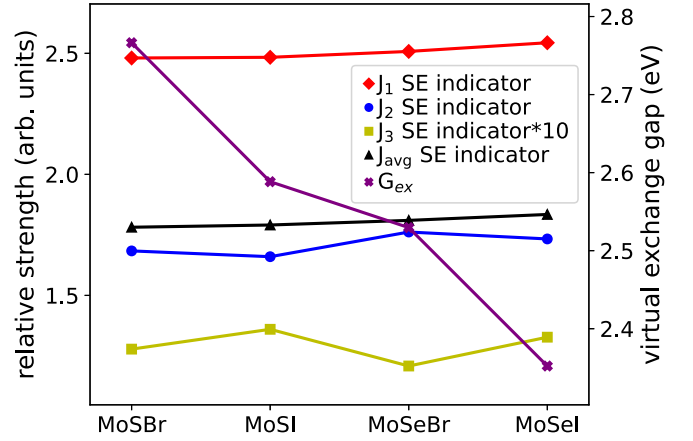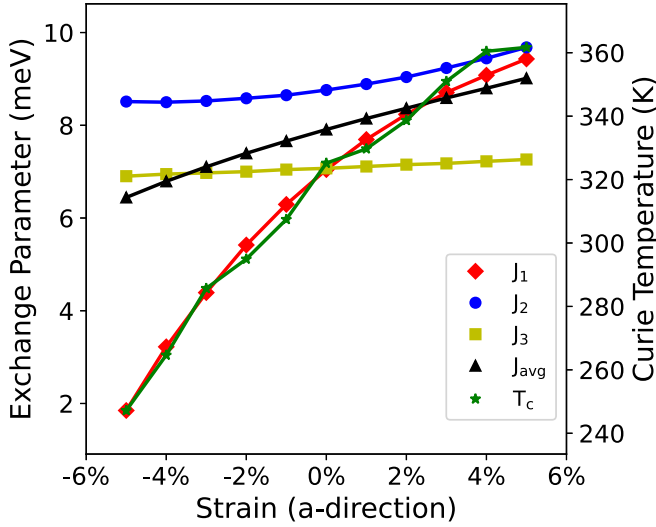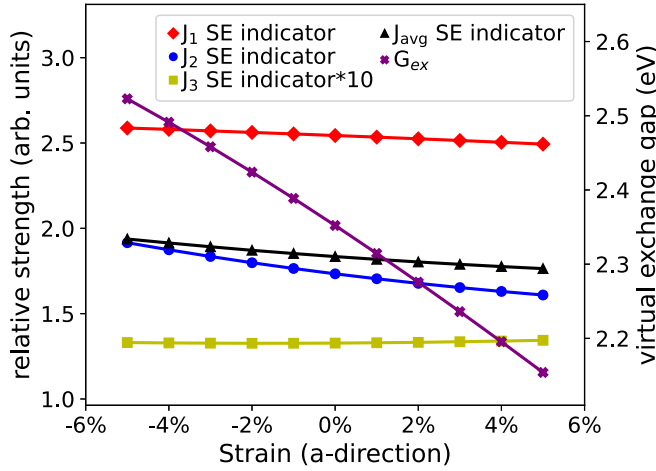

FIG. 3. Superexchange interaction strength indicators and virtual exchange gaps for MoXY monolayers.

for the involved atomic orbitals pertinent to J_1 and J_2 slightly change when varying ligands (cf. Fig. S8 in the Supplemental Material). The resulting $J_1^{\text{SE,ind}}$ and $J_2^{\text{SE,ind}}$ for MoXY monolayers are shown in Fig. 3, and their trends are in excellent agreement with the corresponding exchange interaction parameter in Table III. For each monolayer, $J_1^{\text{SE,ind}}$ is systematically larger than $J_2^{\text{SE,ind}}$, while J_1 is always smaller than J_2. This seemingly discrepancy can be attributed to the fact that the direct exchange interactions pertinent to J_1 are stronger and thus undermines more the contributions from the superexchange interactions. Note that the direct exchange interactions resulting in AFM are expected to be weakened as the cation-cation distances increase. At variance with J_1 and J_2, the contributions from direct exchange interactions to J_3 are expected to be negligible mostly because of the quite small t_{2g} orbital overlapping along the b axis. The orbital overlapping is found to be $\sim$40 (30) times smaller than that for J_1 (J_2). Despite superexchange interactions in J_1 and J_2 being stronger, they are undermined by stronger direct exchange interactions at the same time (see Supplemental Material [43]). This could explain why J_3 is on the same order with the other two parameters but $J_3^{\text{SE,ind}}$ is relatively smaller. The intermediate cation-anion-cation angles are 157.0°, 156.6°, 158.2°, and 157.4° for MoSBr, MoSI, MoSeBr, and MoSeI, respectively. In the vicinity of critical angles where magnetic phase transitions between AFM and FM occur, larger intermediate angles usually result in weaker AFM or stronger FM usually, which means less positive or more negative exchange interaction parameters [50]. We find that J_3 in Table III and $J_3^{\text{SE,ind}}$ for MoXY (except MoSeI) follow this trend. For either MoSeBr or MoSeI, $J_3^{\text{SE,ind}}$ is expected to be overestimated due to approximation in the exchange integral as discussed before. Roughly speaking, when applying the ligand modulation strategy, the superexchange interactions are strengthened and the direct exchanges interactions are weakened for heavier ligands and enhance the Curie temperatures. The more affected term is $p_\sigma - e_g$ covalency rather than the $p_\sigma - t_{2g}$ exchange integral. This is why other indicators relating to $p_\sigma - e_g$ covalency, such as virtual exchange gaps [5] and integrated unoccupied e_g states [21], can to some extent explain the effects of ligand modulation on the overall superexchange interaction strength,
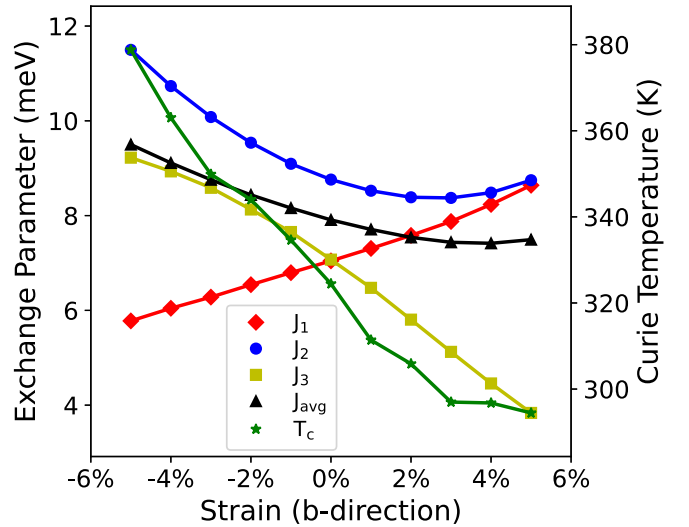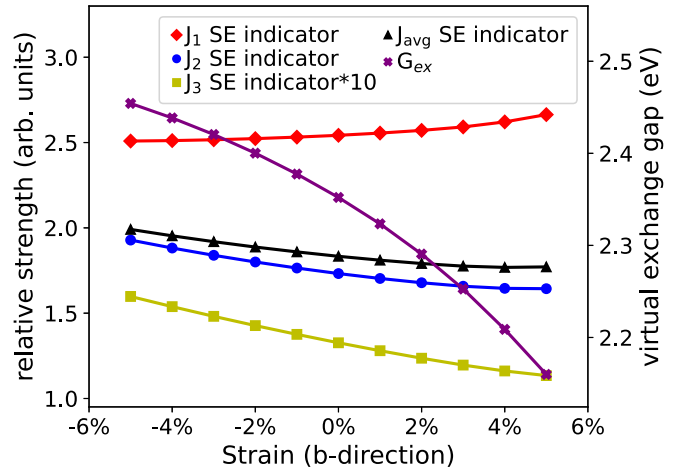
FIG. 4. (a) Exchange interaction parameters, Curie temperatures, and (b) superexchange interaction strength indicators and virtual exchange gaps in MoSeI as functions of the uniaxial strain along the a axis.

FIG. 5. (a) Exchange interaction parameters, Curie temperatures, and (b) superexchange interaction strength indicators and virtual exchange gaps in MoSeI as functions of the uniaxial strain along the b axis.

which corresponds to $J_{\text{avg}}^{\text{SE,ind}}$ in this paper. But note that the trend related to the ligand modulation strategy is not always true.

For MoXY monolayers, their Curie temperatures can be tuned by in-plane biaxial strain. As shown in Figs. 4 and 5, either the tensile strain along the a direction or the compressive strain along the b direction can enhance the Curie temperatures. The behaviors of the three exchange parameters under uniaxial strain along the a or b axes are similar among MoXY (cf. Fig. 4 and Fig. S6 in the Supplemental Material) and CrSBr [54] monolayers, which clearly indicates that these trends have the same physical origin. For tensile strains along the b axis, both virtual exchange gaps G_{ex} (cf. Fig. 5) and integrated occupied e_g states (cf. Fig. S7) indicate increasing superexchange interaction strength, which clearly contradict the decreasing Curie temperatures. Under two types of uniaxial strain, the evolution of $Q_{\text{ET}}(e_g)$ and relevant orbital overlaps are shown in Figs. S7 and S8 in the Supplemental

Material [43]. By using the superexchange strength indicator defined in Eq. (2), we could explain the trends of the three exchange parameters under the two types of uniaxial strain. Uniaxial strains are applied to disentangle the strain effects from two in-plane directions. From Fig. 4(b), the tensile strain along the a axis slightly enhances the superexchange strength for J_3 but decreases for J_1 and J_2. For the tensile strain along the a axis, the direct exchange interactions for J_1 decay more quickly than for J_2 due to more rapidly increasing cation-cation distances, which result in a significant increase in J_1 and slightly increase for J_2 (cf. Fig. 4). For J_2, it can be inferred that the changes in direct exchange interactions prevail those in superexchange interactions. As for J_3, the direct exchange interactions along the b axis remain unchanged, so J_3 follows the same trend with the corresponding superexchange strength indicator $J_3^{\text{SE,ind}}$. As shown in Fig. 5, both J_1 and $J_1^{\text{SE,ind}}$ increase with the tensile strain along the b axis because the contributions from direct exchange interactions are not

TABLE IV. The SOC-MA, shape-MA and total-MA (in μeV) per Mo atom for MoXY (X = S, Se; Y = Br, I) monolayer when taking the b direction as reference.

		[010](b)	[100](a)	[001](c)
MoSBr	SOC-MA	0	1131	532
	Shape-MA	0	−8	56
	Total-MA	0	1123	588
MoSI	SOC-MA	0	1091	887
	Shape-MA	0	−6	60
	Total-MA	0	1085	947
MoSeBr	SOC-MA	0	548	551
	Shape-MA	0	−9	51
	Total-MA	0	539	602
MoSeI	SOC-MA	0	725	729
	Shape-MA	0	−7	47
	Total-MA	0	718	776

changed with the strain. As for J_2 and J_3, both of them follow the same trend with the corresponding indicators, which can be attributed to changes in superexchange interactions being dominant. $J_3^{\mathrm{SE,ind}}$ is overestimated for the tensile strain along the b axis with a larger cation-anion-cation angle for the same reason as discussed before.

D. Magnetic anisotropy energy

We then address the MAE for the monolayer MoXY. The contributions from the spin-orbit coupling (SOC) to the MAE, referred to as SOC-MA, are obtained from noncollinear magnetism calculations in which the spin directions are varied. In addition to SOC-MA, the shape anisotropy originating from magnetic dipole-dipole interactions also contribute to the MAE (referred to as shape-MA), which can be expressed as [54,55]

$$E^{\mathrm{MDD}} = \frac{1}{2}\frac{\mu_0}{4\pi}\sum_{i,j}^{N}\left[\frac{\vec{M}_i \cdot \vec{M}_j}{r_{ij}^3} - 3\frac{(\vec{M}_i \cdot \vec{r}_{ij})(\vec{M}_j \cdot \vec{r}_{ij})}{r_{ij}^5}\right], \quad (5)$$

where $\vec{M}_i$ is the magnetic moment of the TM ion (Mo^{3+}) at site i and r_{ij} denotes the distance between the two sites labeled as i and j. The summation runs over all the neighboring sites within 12 Å, which is sufficiently large to ensure the convergence. By adding shape-MA to SOC-MA, the calculated MAE per unit cell corresponding to the three main crystallographic axes are given in Table IV. Clearly, the magnetic anisotropy in the monolayer MoXY is strongly

triaxial and the contribution from SOC is always dominant in each case. For MoSBr and MoSI, the easy, intermediate, and hard axes are the b, c, and a axes, respectively, while for MoSeBr and MoSeI, the intermediate and hard axes are a and c axes, respectively. The determined easy axis is within the ab plane, indicating that it falls into the category of a 2D XY-type FM magnet with quasi-long-range magnetic order below the Curie temperature. Notably, the MAE in MoXY monolayers are nearly ten orders of magnitude stronger than that in CrSBr [55], indicating the magnetic ordering is more robust, which is critical for application in memory devices and spintronics. The large MAE in monolayer MoXY is attributed to the large SOCs for the heavy Mo-4d and halogen atoms [56,57].

IV. CONCLUSIONS

In summary, we computationally predicted a class of 2D vdW FM semiconductors MoXY with high Cuire temperatures (ranging from 290 K to 322 K) and large magnetic anisotropic energies. The dynamical and thermal stabilities of Mo XY were confirmed by DFPT and AIMD calculations, respectively. The unique quasi-1D electronic transport behavior observed in Mo XY and CrSBr monolayers were explained in terms of tight-binding models and superexchange interactions. We proposed a path-resolved strength indicator for superexchange interactions based on the Kanamori's mechanism. Then, we use the indicator to study the mechanisms of modulating the superexchange interactions in Mo XY through the two heavily used strategies, i.e., ligand modulation and strain engineering. Our study provides insights into enhancing FM couplings and Curie temperatures for 2D FM semiconductors through rationally modulating superexchange interactions, which are critical for their applications in spintronics.

[1] A. K. Geim and K. S. Novoselov, Nat. Mater. **6**, 183 (2007).

[2] S. Manzeli, D. Ovchinnikov, D. Pasquier, O. V. Yazyev, and A. Kis, Nat. Rev. Mater. **2**, 17033 (2017).

[3] M. Gibertini, M. Koperski, A. F. Morpurgo, and K. S. Novoselov, Nat. Nanotechnol. **14**, 408 (2019).

[4] K. F. Mak, J. Shan, and D. C. Ralph, Nat. Rev. Phys. **1**, 646 (2019).

[5] C. Huang, J. Feng, F. Wu, D. Ahmed, B. Huang, H. Xiang, K. Deng, and E. Kan, J. Am. Chem. Soc. **140**, 11519 (2018).

[6] J. F. Sierra, J. Fabian, R. K. Kawakami, S. Roche, and S. O. Valenzuela, Nat. Nanotechnol. **16**, 856 (2021).

[7] N. P. Wilson, K. Lee, J. Cenker, K. Xie, A. H. Dismukes, E. J. Telford, J. Fonseca, S. Sivakumar, C. Dean, T. Cao, X. Roy, X. Xu, and X. Zhu, Nat. Mater. **20**, 1657 (2021).

[8] X. Jiang, Q. Liu, J. Xing, N. Liu, Y. Guo, Z. Liu, and J. Zhao, Appl. Phys. Rev. **8**, 031305 (2021).

[9] N. D. Mermin and H. Wagner, Phys. Rev. Lett. **17**, 1133 (1966).

[10] P. C. Hohenberg, Phys. Rev. **158**, 383 (1967).

[11] X. Li, T. Cao, Q. Niu, J. Shi, and J. Feng, Proc. Natl. Acad. Sci. **110**, 3738 (2013).

[12] N. Sivadas, M. W. Daniels, R. H. Swendsen, S. Okamoto, and D. Xiao, Phys. Rev. B **91**, 235425 (2015).

[13] B. L. Chittari, Y. Park, D. Lee, M. Han, A. H. MacDonald, E. Hwang, and J. Jung, Phys. Rev. B **94**, 184428 (2016).

[14] N. Mounet, M. Gibertini, P. Schwaller, D. Campi, A. Merkys, A. Marrazzo, T. Sohier, I. E. Castelli, A. Cepellotti, G. Pizzi, and N. Marzari, Nat. Nanotechnol. **13**, 246 (2018).

[15] C. Gong, L. Li, Z. Li, H. Ji, A. Stern, Y. Xia, T. Cao, W. Bao, C. Wang, Y. Wang, Z. Q. Qiu, R. J. Cava, S. G. Louie, J. Xia, and X. Zhang, Nature (London) **546**, 265 (2017).

[16] B. Huang, G. Clark, E. Navarro-Moratalla, D. R. Klein, R. Cheng, K. L. Seyler, D. Zhong, E. Schmidgall, M. A. McGuire, D. H. Cobden, W. Yao, D. Xiao, P. Jarillo-Herrero, and X. Xu, Nature (London) **546**, 270 (2017).

[17] M. Lang, M. Montazeri, M. C. Onbasli, X. Kou, Y. Fan, P. Upadhyaya, K. Yao, F. Liu, Y. Jiang, W. Jiang, K. L. Wong, G. Yu, J. Tang, T. Nie, L. He, R. N. Schwartz, Y. Wang, C. A. Ross, and K. L. Wang, Nano Lett. **14**, 3459 (2014).

[18] M. Li, W. Cui, J. Yu, Z. Dai, Z. Wang, F. Katmis, W. Guo, and J. Moodera, Phys. Rev. B **91**, 014427 (2015).

[19] C. Gong and X. Zhang, Science **363**, eaav4450 (2019).

[20] Y. Ren, Q. Li, W. Wan, Y. Liu, and Y. Ge, Phys. Rev. B **101**, 134421 (2020).

[21] J. Xiao, D. Legut, W. Luo, H. Guo, X. Liu, R. Zhang, and Q. Zhang, Phys. Rev. B **101**, 014431 (2020).

[22] Z. Jiang, P. Wang, J. Xing, X. Jiang, and J. Zhao, ACS Appl. Mater. Interfaces **10**, 39032 (2018).

[23] X. Yao, L. Wang, Y. Sun, X. Li, J. Sun, B. Wang, M. He, and X. Zhang, Phys. Rev. B **105**, 214421 (2022).

[24] J. Kanamori, J. Phys. Chem. Solids **10**, 87 (1959).

[25] P. Hohenberg and W. Kohn, Phys. Rev. **136**, B864 (1964).

[26] W. Kohn and L. J. Sham, Phys. Rev. **140**, A1133 (1965).

[27] P. Giannozzi, S. Baroni, N. Bonini, M. Calandra, R. Car, C. Cavazzoni, D. Ceresoli, G. L. Chiarotti, M. Cococcioni, I. Dabo, A. D. Corso, S. de Gironcoli, S. Fabris, G. Fratesi, R. Gebauer, U. Gerstmann, C. Gougoussis, A. Kokalj, M. Lazzeri, L. Martin-Samos *et al.*, J. Phys.: Condens. Matter **21**, 395502 (2009).

[28] M. Fuchs and M. Scheffler, Comput. Phys. Commun. **119**, 67 (1999).

[29] J. P. Perdew, K. Burke, and M. Ernzerhof, Phys. Rev. Lett. **77**, 3865 (1996).

[30] A. I. Liechtenstein, V. I. Anisimov, and J. Zaanen, Phys. Rev. B **52**, R5467 (1995).

[31] R. Esteban-Puyuelo, D. D. Sarma, and B. Sanyal, Phys. Rev. B **102**, 165412 (2020).

[32] N. Mishra, B. P. Pandey, B. Kumar, and S. Kumar, Superlattices Microstruct. **160**, 107083 (2021).

[33] S.-H. Kang, S. Jeon, H.-J. Kim, W. Ko, S. Cho, S. H. Kang, S. W. Kim, H. Yang, H. W. Kim, and Y.-W. Son, Phys. Rev. B **105**, 045143 (2022).

[34] Z. Guguchia, A. Kerelsky, D. Edelberg, S. Banerjee, F. von Rohr, D. Scullion, M. Augustin, M. Scully, D. A. Rhodes, Z. Shermadini, H. Luetkens, A. Shengelaya, C. Baines, E. Morenzoni, A. Amato, J. C. Hone, R. Khasanov, S. J. L. Billinge, E. Santos, A. N. Pasupathy *et al.*, Sci. Adv. **4**, eaat3672 (2018).

[35] S. Grimme, J. Antony, S. Ehrlich, and H. Krieg, J. Chem. Phys. **132**, 154104 (2010).

[36] A. Togo and I. Tanaka, Scr. Mater. **108**, 1 (2015).

[37] G. J. Martyna, M. L. Klein, and M. Tuckerman, J. Chem. Phys. **97**, 2635 (1992).

[38] G. Pizzi, V. Vitale, R. Arita, S. BlÜgel, F. Freimuth, G. Géranton, M. Gibertini, D. Gresch, C. Johnson, T. Koretsune, J. Ibañez-Azpiroz, H. Lee, J.-M. Lihm, D. Marchand, A. Marrazzo, Y. Mokrousov, J. I. Mustafa, Y. Nohara, Y. Nomura, L. Paulatto *et al.*, J. Phys.: Condens. Matter **32**, 165902 (2020).

[39] R. F. L. Evans, W. J. Fan, P. Chureemart, T. A. Ostler, M. O. A. Ellis, and R. W. Chantrell, J. Phys.: Condens. Matter **26**, 103202 (2014).

[40] P. Asselin, R. F. L. Evans, J. Barker, R. W. Chantrell, R. Yanes, O. Chubykalo-Fesenko, D. Hinzke, and U. Nowak, Phys. Rev. B **82**, 054415 (2010).

[41] R. F. L. Evans, U. Atxitia, and R. W. Chantrell, Phys. Rev. B **91**, 144425 (2015).

[42] A. D. Corso, Comput. Mater. Sci. **95**, 337 (2014).

[43] See Supplemental Material at http://link.aps.org/supplemental/10.1103/PhysRevB.108.064425 for more details including AIMD simulations, phonon band structure, ingredients for superexchange indicators, etc.

[44] S. Bruzzone and G. Fiori, Appl. Phys. Lett. **99**, 222108 (2011).

[45] S. Takagi, A. Toriumi, M. Iwase, and H. Tango, IEEE Trans. Electron Devices **41**, 2357 (1994).

[46] G. Fiori and G. Iannaccone, Proc. IEEE **101**, 1653 (2013).

[47] Y. Guo, Y. Zhang, S. Yuan, B. Wang, and J. Wang, Nanoscale **10**, 18036 (2018).

[48] C. Wang, X. Zhou, L. Zhou, N.-H. Tong, Z.-Y. Lu, and W. Ji, Sci. Bull. **64**, 293 (2019).

[49] F. Wu, I. Gutiérrez-Lezama, S. A. López-Paz, M. Gibertini, K. Watanabe, T. Taniguchi, F. O. von Rohr, N. Ubrig, and A. F. Morpurgo, Adv. Mater. **34**, 2109759 (2022).

[50] J. B. Goodenough, *Magnetism and the Chemical Bond* (Interscience, Wiley, New York, 1963).

[51] J. B. Goodenough, Phys. Rev. **100**, 564 (1955).

[52] P. W. Anderson, Phys. Rev. **115**, 2 (1959).

[53] J. Murrell and J. Teixeira-Dias, Mol. Phys. **19**, 521 (1970).

[54] F. Xue, Y. Hou, Z. Wang, and R. Wu, Phys. Rev. B **100**, 224429 (2019).

[55] K. Yang, G. Wang, L. Liu, D. Lu, and H. Wu, Phys. Rev. B **104**, 144416 (2021).

[56] A. J. Browne, A. Krajewska, and A. S. Gibbs, J. Mater. Chem. C **9**, 11640 (2021).

[57] F. Herman, C. D. Kuglin, K. F. Cuff, and R. L. Kortum, Phys. Rev. Lett. **11**, 541 (1963).